

# A numerical model for the time-dependent wake of a pedalling cyclist

Martin D Griffith<sup>1</sup>, Timothy N Crouch<sup>1</sup> , David Burton<sup>1</sup>, John Sheridan<sup>1</sup>, Nicholas AT Brown<sup>2,3</sup> and Mark C Thompson<sup>1</sup>

Proc IMechE Part P:  
*J Sports Engineering and Technology*  
1–12

© IMechE 2019

Article reuse guidelines:

sagepub.com/journals-permissions

DOI: 10.1177/1754337119858434

journals.sagepub.com/home/ptp



## Abstract

A method for computing the wake of a pedalling cyclist is detailed and assessed through comparison with experimental studies. The large-scale time-dependent turbulent flow is simulated using the *Scale Adaptive Simulation* approach based on the *Shear Stress Transport* Reynolds-averaged Navier–Stokes model. Importantly, the motion of the legs is modelled by joining the model at the hips and knees and imposing solid body rotation and translation to the lower and upper legs. Rapid distortion of the cyclist geometry during pedalling requires frequent interpolation of the flow solution onto new meshes. The impact of numerical errors, that are inherent to this remeshing technique, on the computed aerodynamic drag force is assessed. The dynamic leg simulation was successful in reproducing the oscillation in the drag force experienced by a rider over the pedalling cycle that results from variations in the large-scale wake flow structure. Aerodynamic drag and streamwise vorticity fields obtained for both static and dynamic leg simulations are compared with similar experimental results across the crank cycle. The new technique presented here for simulating pedalling leg cycling flows offers one pathway for improving the assessment of cycling aerodynamic performance compared to using isolated static leg simulations alone, a practice common in optimising the aerodynamics of cyclists through computational fluid dynamics.

## Keywords

Cycling, unsteady aerodynamics, wake dynamics, mesh deformation, turbulent flows

Date received: 27 April 2018; accepted: 4 May 2019

## Introduction

Elite cycling is a sport in which aerodynamic drag plays a particularly important role. At racing speed, 90% of the resistance experienced by the cyclist is attributable to aerodynamic drag.<sup>1,2</sup> Even small reductions in drag (i.e. reducing the frontal area of the cyclist body, tailoring the cyclist's clothing or optimising rider configurations for drafting in team events) can easily change a race outcome. This potential for drag reduction to affect race results has motivated fluid dynamics researchers to investigate the problem.

Previous studies have detailed the significant variations of drag with drafting, crosswinds and cyclist's body position, using wind-tunnel experiments and numerical simulation.<sup>3–10</sup> Crouch et al.<sup>11</sup> experimentally investigated the wake topology and drag experienced by the rider as it varies with the pedalling phase or crank angle. Using wind-tunnel measurements, they identified variations of 15% in drag depending on leg position. The pedalling phases for the high- and low-drag positions corresponded to the following: one leg

being stretched out straight with the other tucked up to the torso, and each thigh being at the same angle relative to the torso. Investigations were also conducted on the rich topology of the wake, including strong vortex generation from the torso and the variations in pressure across the cyclist's back. The study by Griffith et al.,<sup>12</sup> from which this study largely follows, investigated the same problem computationally, finding the same variation in drag with leg position. In the study, the wake was investigated in detail for the crank angle cases exhibiting low and high drag.

<sup>1</sup>Department of Mechanical and Aerospace Engineering, Monash University, Clayton, VIC, Australia

<sup>2</sup>Australian Institute of Sport, Canberra, ACT, Australia

<sup>3</sup>Faculty of Health, University of Canberra, Canberra, ACT, Australia

### Corresponding author:

Mark C Thompson, Department of Mechanical and Aerospace Engineering, Monash University, Clayton, VIC 3800, Australia.

Email: mark.thompson@monash.edu

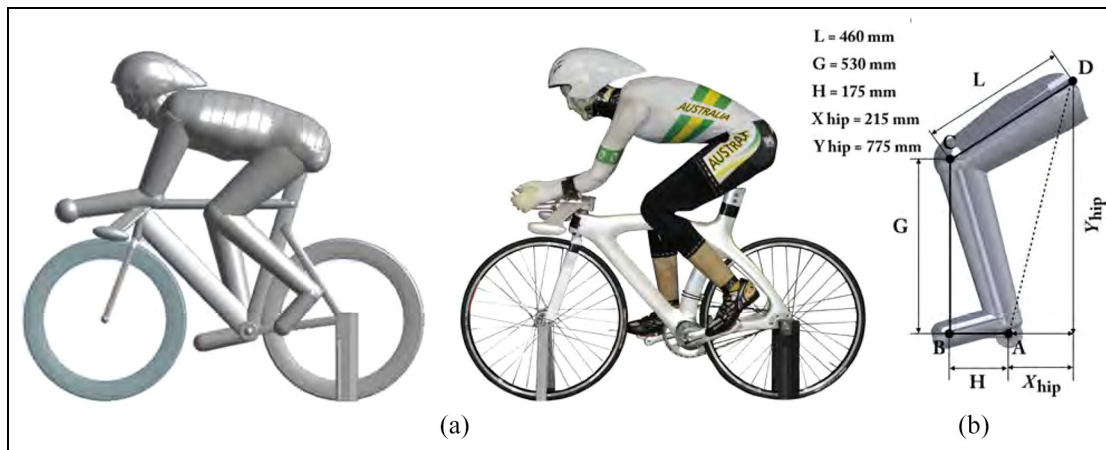


**Figure 1.** (a) A comparison of the numerical model position with that of the experimental mannequin, at a crank angle of  $\theta = 15^\circ$ . (b) Major dimensions of the leg that determine the motion of the leg around the crank cycle. Corresponding arm dimensions include the shoulder to elbow and elbow to hand lengths, which are 410 and 415 mm, respectively.

A common aspect to all these studies is the adoption of a static cyclist model, that is, the legs being fixed at the given phase/crank angle. Investigating the flow with a static model presents an obvious starting point for a computational or experimental fluid dynamics study of cycling aerodynamics. However, given the large change in the wake structure between low- and high-drag leg positions, optimising aerodynamics for one leg position will not necessarily result in a net drag reduction when the leg position continuously varies over the crank cycle. In addition to this, recent studies<sup>13</sup> show that while the time-averaged aerodynamic drag force is not significantly affected by pedalling frequency, the instantaneous drag force around the crank cycle is affected. This was found to be primarily a result of differences in the aerodynamic drag force acting on the left and right legs due to the back and forth pumping motion of the legs around the crank cycle. Clearly, multiple phases of the crank cycle must be considered when targeting a net drag reduction over a full rotation of the crank cycle.

For a computational fluid dynamics (CFD) study incorporating leg movement, in terms of managing model and mesh deformation, the pedalling cyclist also presents an extremely challenging problem. To date, there are no studies reported in the literature that the authors are aware of that attempt to simulate the dynamic leg motion. The large-scale deformation, the independent motions of thighs and calves of the model with respect to the torso, and the interaction of body surfaces at the hip and knees, and the need to resolve boundary layer flows, make the most common methods of handling body movement in a CFD simulation unsuitable. These problems make adopting a static model attractive, but implicitly assume that the data and conclusions obtained from static-model experiments and simulations will apply to the dynamic model, both generally and instantaneously at the corresponding crank angle phase.

In this study, details of a CFD simulation of flow past a cyclist, at full scale and at racing speed, incorporating the motion of the legs are presented. The magnitude of the primary sources of numerical errors which arise due to the remeshing technique used to simulate leg motion is detailed. The geometry of the numerical model and simulated pedalling frequency are similar to the wind-tunnel model used by Crouch et al.,<sup>13</sup> allowing for a semi-quantitative comparison between both experimental and numerical data sets.

## Methodology

### Model details

The numerical model of the rider is similar to the dimensions of the experimental mannequin of Crouch et al.,<sup>11</sup> from which the major geometric details can be found. Figure 1 compares the numerical rider geometry with the mannequin form used in experiments. The leg position throughout the crank cycle is described relative to a reference crank angle,  $\theta = 0^\circ$ , located where the left crank is at its furthest position downstream or, alternatively, where the pedals are level and the right pedal is towards the front of the bicycle.

Having a well-defined and controlled jointed computer-aided design (CAD) model consisting of defined components allows the geometry to be manipulated dynamically, enabling torso- and arm-angle adjustment, and, importantly for this study, to incorporate pedalling leg motion. Hence, the torso, arm and leg geometries were created from simplified shapes using CAD software, but with enough detail to capture the essential geometric features of these components. The bicycle used experimentally was not recreated numerically; rather, a generic bicycle model was generated, with the sections and major dimensions representative of a standard track bicycle. Small-scale geometric

features, such as the spokes, have also been omitted, as have the chain rings, chain, and pedals; however, the cranks are included.

The cyclist and bicycle geometry used in the numerical model are only approximations to the mannequin and bicycle used for the wind-tunnel tests. At the time of the study, access was not available to a surface scanning capability that would have allowed better fidelity of the numerical surface model. Despite this limitation, one of the main aims of this research was to quantify the differences induced by leg movement relative to the static numerical model, with the related experimental measurements providing a degree of validation.

From the outset, the goal in building the computational model was to achieve a geometrically dynamic CFD simulation that was capable of capturing the large variation in drag observed for a pedalling cyclist. Essentially, the CFD model needed to be capable of producing any geometry over the 360° range of the crank angle cycle. This requires precise solid body rotation and translation of the thighs and calves, which are more readily defined and moved within a CAD model than in a three-dimensional (3D) scan. Figure 1 also defines the dimensions of the legs, which determine the motion of the upper and lower legs around the hip and crank. For this study, the motion of the legs was simplified by fixing the ankle joint, with the foot perpendicular to the calf. This is a reasonable approximation in practice and is also consistent with the experimental set-up used for comparison.

Once the motion is defined, the large translation, rotation and intersections of the leg components present particular challenges for a successful CFD simulation. In terms of the motion, there are five components: two calves, two thighs, and the fixed torso, head, arms and bicycle. Accelerating frames of reference are unsuitable due to the independent motions of the five components. The complex intersections of the five components at the knees and hips mean that sliding mesh interface methods are also not feasible. An immersed boundary method fluid solver could handle the component motion, but there is currently no well-tested strategy for dealing with turbulent boundary layers at high Reynolds numbers in an immersed boundary setting. Grid deformation is the option used in this study. There are studies of surface meshes being manipulated for deformation, for example, in dolphin-like swimming motions;<sup>14</sup> however, the flexing rider knee and pressing of the thigh into the rider torso mean that the surface deformations at the points of intersection are difficult to account for.

In the model, surfaces effectively appear and disappear into one another; grid points are rapidly stretched or squashed at the intersection points, severely limiting the extent to which the crank angle can be advanced and the mesh deformed, without the simulation failing. For that reason, frequent interpolation of the flow solution onto a new undeformed mesh is required to avoid the creation of elements of negative volume at the intersection points.

At some crank angles, the tolerance for deformation is low. For instance, at a crank angle of  $\theta \approx 75^\circ$ , the left thigh pressing into the torso results in a folded mesh within a crank angle rotation of 1.6°. By contrast, at  $\theta \approx 105^\circ$ , where the left thigh is opening away from the torso, the mesh folds after a crank angle rotation of 4.2°. Despite the variability of the extent to which meshes could deform, a constant solution interpolation frequency was chosen for the entire crank angle cycle, with one interpolation per one degree of crank angle rotation. This compromise ensured the simulation could reliably advance every degree through the pedalling cycle, at the price of more regular solution interpolation in certain phases of the cycle than was perhaps strictly necessary to avoid catastrophic mesh distortion. However, this compromise was important, as it conferred a consistency and regularity to the method around the crank angle cycle, allowing a more systematic approach to the mesh movement/remeshing task while minimising the extent to which the simulation required manual intervention during critical phases of the cycle.

Thus, the computation required construction of meshes at each degree of the cycle. In total, 180 CAD models representing crank angle positions from 75° to 254° were constructed and then systematically and carefully meshed. The simulation was then run through 180° of the crank cycle as proof of concept. Once this was achieved, the meshes for the remaining half of the crank angle cycle were generated based on mirrored images of the preceding 180 models. Considerable care was required in the generation of each individual mesh to ensure mesh quality and adequate resolution in critical region while incorporating sufficient resolution at the boundaries. Each mesh consisted of approximately 33 million cells. Over the surface of the rider, surface grid sizes were set at 0.005 m. As is recommended for separated flows, boundary layers were resolved down to the wall with  $y^+ < 1$  over the cyclist body. Note that the cell numbers and mesh point distributions of the meshes are based on meshes used for the static leg cases that underwent resolution studies and grid sensitivity tests to verify reasonable grid independence (within 2%) of the predictions.<sup>12</sup>

### Numerical simulation

Numerical flow fields were simulated at a freestream velocity of  $U = 16$  m/s and a pedalling frequency ' $f$ ' of 1.39 Hz. This corresponds to a reduced pedalling frequency shown in equation (1)

$$k = \frac{2r\pi f}{U} = 0.092 \quad (1)$$

where ' $r$ ' is the length of the crank (0.175 m in this case). These cycling conditions were targeted in this study to match those corresponding to the experimentally obtained data set used for comparison.

Flows were simulated with commercial CFD software, ANSYS-CFX, which employs a conservative second-order finite-volume based method. A description of the model and results for both static-model Reynolds-averaged Navier–Stokes (RANS) simulations and static-model transient simulations using the Scale Adaptive Simulation–Shear Stress Transport (SAS-SST) model of Menter and Egorov<sup>15</sup> are presented in Griffith et al.<sup>12</sup> The numerical results for a dynamic pedalling cyclist presented in this article were also obtained using SAS-SST transient simulations. In near-wall regions, the SAS-SST solver reduces to the same treatment and mesh requirements as the (unsteady) SST-RANS model, while in unsteady regions of the flow (such as in separated flow in the cyclist wake) the turbulent length scale is automatically reduced to approach large eddy simulation (LES)-like behaviour; the range of length and time scales captured depends on the local cell size and timestep. Thus, unsteady flow features, including large-scale turbulent motions, can be modelled down towards the grid resolution. Unsteady flow resolved at smaller scales can then influence flow behaviour at larger scales, which can be important for capturing the correct large-scale wake flow behaviour. While the model attempts to capture the large-scale unsteady wake features, the SST-RANS model is used near surfaces to predict unsteady separation. Comparisons to standard LES wake predictions and experiments for some generic aerodynamic cases, such as flow over a cavity and a jet in a crossflow, can be found in previous studies.<sup>16,17</sup> The approach is only recommended for strongly separated globally unstable wakes, where strong self-sustaining instabilities control the large-scale wake features that dominate wake spatial development and frequency content, which is the case here.

Figure 2(a) shows the domain boundaries which, except for the road, were placed far enough from the cyclist that they had a negligible effect on the simulated results. The road, represented by the lower domain boundary, was modelled as a wall with a velocity matching the freestream velocity,  $U$ . A zero-velocity condition was applied to the rider and bicycle, including the tyres. The rotation of the tyres was not included in this initial model, noting that the main objective was to examine the effect of movement of the cyclist's legs. The inlet was placed 10 m upstream of the rider, while the remaining top and side boundaries were also set 10 m from the rider. This resulted in a blockage ratio of approximately 0.2%. The outlet length was set at 40 m. Solutions with even larger clearances between the rider and the domain boundaries produced negligible differences in the flow near the cyclist. The sensitivity of the solution to mesh resolution was tested by running the method on higher density meshes and by verifying the flow predictions against experimental measurements, with further details given in Griffith et al.<sup>12</sup>

A timestep of  $4 \times 10^{-4}$  s was employed; this timestep was determined from the author's previous work with

transient SAS-SST simulations with static models.<sup>12</sup> With a pedalling frequency of 1.389 Hz, or 0.72 s per pedalling period, this corresponds to five timesteps per degree of crank angle, or per mesh, and 1800 timesteps per period. The simulation was run in parallel on 64 nodes, using high-performance computing hardware at the National Computational Infrastructure (NCI) National Facility in Canberra, Australia. On 64 nodes, each degree of the simulation took approximately 45 min to run, equivalent to approximately 20,000 CPU-hours per pedalling cycle. The simulation was initialised with the flow from an SAS-SST simulation run at crank angle  $\theta = 75^\circ$ . Results were recorded two pedal cycles after simulation startup to allow any transient effects to advect out of the computation domain. Following the simulation initiation stage, flow fields and aerodynamic forces were recorded for a duration of seven pedal strokes.

## Results and discussion

### The remeshing technique

The numerical method used to simulate the leg motion introduces a small degree of non-physical noise into the simulation, which is compounded by the fact that a turbulent flow with highly resolved boundary layers is being simulated. It is impossible to have the resultant configuration from a deformed mesh exactly match the configuration of the undeformed mesh at the next crank angle, so some disturbance is to be expected. The motion of the surfaces of the legs combined with the remeshing onto slightly different surface meshes has the potential to perturb the boundary layer region, although it should be remembered that in those regions, small-scale turbulence structures are not modelled directly, and the meshes have been carefully constructed to fully resolve the (mean) velocity gradients within the boundary layers. In this section, two different strategies are described to assess the numerical error, or at least its effect on the bulk flow, associated with the remeshing and the interpolation technique. The first method involves varying the rate at which remeshing occurs and analysing differences in simulated variables. The second involves comparison of the computed drag-area time series obtained from static leg transient and dynamic leg simulations.

Figure 2(b) plots the drag-area time signal using two different interpolation strategies, one being the strategy used in findings presented in this study where the remeshing occurs every  $1^\circ$  and another where the simulation is remeshed every  $4^\circ$ . As in previous works, the authors define drag area as shown in equation (2)

$$C_D A = \frac{D}{\frac{1}{2} \rho U^2} \quad (2)$$

where  $D$  is the drag force,  $\rho$  is the density of air and  $U$  is the freestream velocity. The simulation restarting

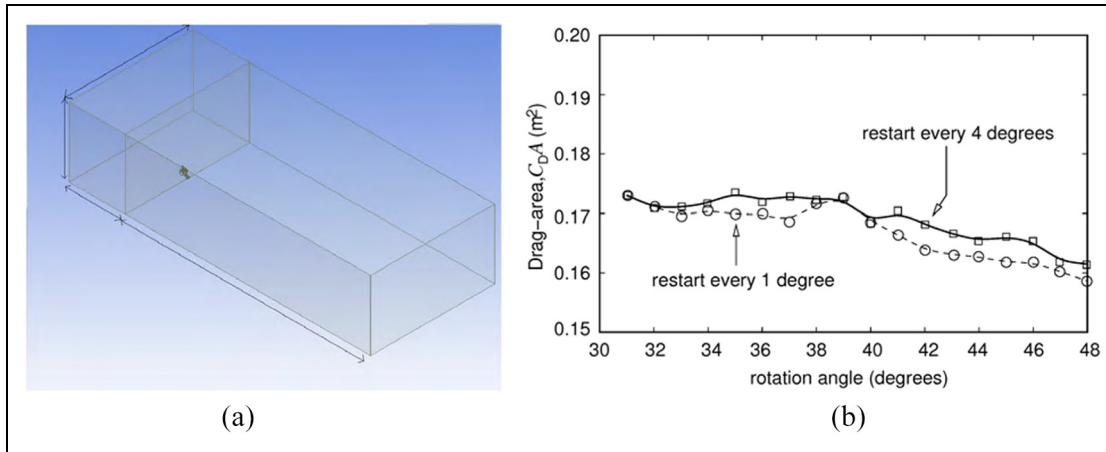


**Figure 2.** (a) Image showing the computational domain. (b) Plot of the drag-area time signal, comparing the main simulation, restarting every  $1^\circ$  of crank angle rotation, with another simulation restarting every  $4^\circ$ . The drag is plotted every five timesteps.

every  $4^\circ$  of rotation, thereby reducing the effect of the interpolation error, albeit increasing the error due to grid skewness and mesh distortion, can be seen to follow the same path as the more regularly restarted simulation, although there are some differences for this highly turbulent flow. Quantitatively, the comparison indicates that the drag signal difference caused by regular remeshing is typically within 2% or less of the signal produced with less frequent remeshing. This should be compared with the drag variation over a cycle, which is one order of magnitude larger.

Based on a quasi-steady assumption, which has been shown to be a reasonable approximation in previous works for the pedalling frequencies under investigation here, one would expect that the time-varying nature of the dynamic results would still reflect that of static leg time signals. Figure 3(a) plots the time signal of  $C_{DA}$  for the dynamic simulation and for two simulations with static models, with crank angle  $\theta = 15^\circ$  and  $\theta = 75^\circ$  for the low- and high-drag cases, respectively. The high-frequency noise of approximately 500 Hz in the drag-area signal from the dynamic simulation due to the high frequency at which the solution is interpolated onto a new mesh is evident. This noise is exacerbated for the drag signal because it depends on the accuracy of the pressure field near moving surfaces, where velocity gradients are highest and hence the interpolation errors are likely to be largest.

In an attempt to remove some of the high-frequency interpolation noise seen in the drag-area signal, Figure 3(b) replots the data from Figure 3(a), but filtered to reduce high-frequency noise. This is achieved by applying a  $4 \times 10^{-3}$  s running average to the raw signal. This averaging period corresponds to twice the remeshing period (i.e. 10 timesteps or  $2^\circ$  in crank angle) in an attempt to reduce the noise introduced by frequent remeshing. Remeshing tends to cause spikes in the pressure signal as the pressure has to adjust at the moving boundary to correct mass conservation caused by interpolation. After each interpolation step, this pressure

oscillation about the mean signal is damped over the next couple of timesteps, suggesting that a running average will help remove this noise. Indeed, this averaging largely removes the 500-Hz remeshing noise, and the reprocessed signal begins to resemble that of the static cases, in terms of fluctuation amplitudes and frequencies seen, especially in the high-drag signal.

Based on the drag-area signal of the dynamic model in Figure 3(b), a large variation of drag area with crank angle is present. Despite interpolation noise introduced into the dynamic simulation, a reprocessed drag-area signal is produced that is consistent with static leg position findings. This is examined further below. Of some interest is that the mean of the dynamic signal is relatively close to the low-drag static signal, suggesting there is a nonlinear effect of pedalling on the flow state, causing an average closer to the minimum drag of a non-pedalling cyclist rather than the mean.

### Comparison with experimental results

To assess whether the dynamic leg simulations have captured the essential flow physics responsible for the large variation in drag throughout the crank cycle, the authors compared both computed results of aerodynamic drag and wake flow fields with the experimental studies.<sup>13</sup> First, computed  $C_{DA}$  results were compared with results obtained from experiment. Figure 4 plots phased averaged drag area values from this study (averaged over seven cycles) and the experimental study at the same reduced pedalling frequency shown only for the second half of the crank cycle for clarity. The maximum and minimum values of computed  $C_{DA}$  over the seven cycles are also plotted as fainter lines above and below the average signal. This provides an indication of the variability of the signal from one cycle to the next. Also shown are the  $C_{DA}$  results of static leg simulations (steady-state RANS and time-averaged transient static leg simulations) and static leg  $C_{DA}$  results obtained from experiment.

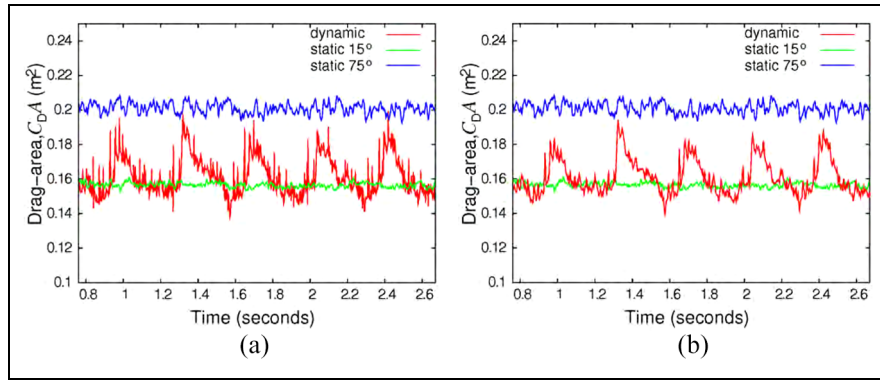


**Figure 3.** (a) Plot of the drag area time signal,  $C_{DA}$ , for three transient simulations: one with a dynamic model, one with a static model at  $15^\circ$  and one with a static model at  $75^\circ$ , and (b) the same plot as (a), but with a  $4 \times 10^{-3}$  s (10 timesteps) running average used to suppress the interpolation noise for the dynamic cases.

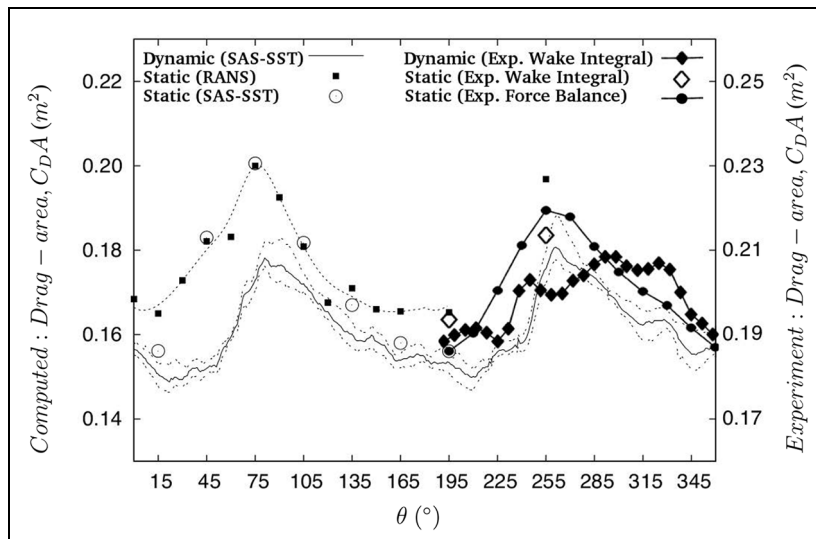


**Figure 4.** A summary of the drag areas,  $C_{DA}$ , returned using different methodologies, over the crank angle cycle. For the dynamic simulation, the phase-averaged  $C_{DA}$  is plotted, with the maximum and minimum drag areas measured for different pedalling cycles plotted above and below the average signal in dashed lines. Solid squares plot the drag area returned by steady-state RANS calculations with static leg models, for  $0^\circ \leq \theta \leq 255^\circ$ .<sup>12</sup> Hollow circles are converged time averages of the drag signal from transient simulations with static legs, for  $15^\circ \leq \theta \leq 165^\circ$ . Equivalent experimental results<sup>13</sup> are plotted for the second half of the crank cycle for clarity. Note. The experimental  $C_{DA}$  results have been scaled to match the area of the numerical model.

Comparing both data sets, the simulated  $C_{DA}$  values are  $\approx 15\%$  lower than the experimental findings, primarily as a result of simplifications to the geometry of the numerical model. Despite this, the variation in the  $C_{DA}$  across the crank cycle, which is of primary importance to this study, is replicated in both data sets. For static leg  $C_{DA}$  results, both numerical and experimental data sets show a variation in  $C_{DA}$  of  $\approx 15\% - 20\%$  with the peak drag occurring at the high-drag  $\theta = 75^\circ$  and  $\theta = 255^\circ$  crank angles when the hip angle of the left or right leg is at its most open position.

Comparing static and dynamic results, both numerical simulations and experimental results show the largest variation in  $C_{DA}$  drag leg positions. For the low-drag near-symmetrical leg positions at approximately

$15^\circ$  and  $195^\circ$ , the variation in  $C_{DA}$  between static and phase-averaged  $C_{DA}$  is small. As described previously,<sup>12</sup> the time-averaged SAS-SST transient simulations are better able to capture the time-averaged drag force for this portion of the crank cycle where the flow is highly unstable compared to the asymmetric leg positions/state. The reduction in the peak drag around the high-drag leg positions is similar for both numerical model and experiments. This reduction is attributed to the asymmetric back-and-forth pumping motion of the legs and has previously been likened to a phase off-set and redistribution of the aerodynamic drag force to latter phase of the crank cycle.<sup>13</sup> Although the numerical results do show the phase-averaged drag signal approaching the static  $C_{DA}$  results immediately

following the high-drag leg position (between  $90^\circ$  and  $165^\circ$ ), they do not exceed the static results as is observed from experiment in the opposite second half of the cycle.

Despite these differences in numerical and experimental findings, the primary trends in the variation of drag area with crank angle between the static and dynamic cases are consistent with what is known of the flow structure, which is discussed in the following sections, and not a result of numerical error introduced by the dynamic leg motion and remeshing.

### Convection velocity estimate

In Griffith et al.,<sup>12</sup> downstream data were compared between experimental results<sup>11</sup> and from computational simulations, all using static cyclist models. However, a complication arises in making similar downstream comparisons with the dynamic model: there exists a convection velocity for the flow structures shedding in the wake of the cyclist. If one were to compare the flow downstream for the time-averaged SAS-SST solution to a snapshot of the dynamic flow, one must consider that the structures shedding from the cyclist at that crank angle will take time to reach the downstream station. Therefore, for data taken downstream of the model, a phase lag,  $\theta_l$ , is calculated, as shown in equation (3)

$$\theta_l = \left( \frac{lf}{u_c U} \right) \times 360 \quad (3)$$

where  $l$  is the distance downstream,  $f$  is the pedalling frequency and  $u_c$  is the non-dimensionalised convection velocity.

There are a wide range of methods for measuring convection velocity. The cyclist wake is dominated by streamwise vortices, so this investigation of convection velocity focuses on planes perpendicular to the free-stream velocity, where the streamwise vorticity topology is more easily analysed.

Figure 5(a) and (b) plots the time-averaged vorticity fields downstream for flows past static cyclist geometries with  $\theta = 15^\circ$  and  $\theta = 75^\circ$ , as found in Griffith et al.<sup>12</sup> To estimate the convection velocity, the method proposed is to find an average of the time-averaged velocity within the vortex cores observable in Figure 5. A strict definition for the edge of a vortex does not exist. Hence, the determination of the vortex boundary and convection velocity is subject to interpretation. The major vortex pairings are of principal interest, and the authors would like to determine the behaviour of the large vortex pairings with a pedalling model; therefore, the determination of the vortex boundary is necessarily guided by a qualitative assessment of the vorticity field. The green contour of streamwise vorticity magnitude visible in Figure 5(a) and (b) approximates the regions of the large-scale vortex behaviour. These are the vortices of interest, so the convection velocity is taken from

an average of the streamwise velocity within this contour. Figure 5(c) plots the returned convection velocity estimate across several downstream stations and at six cranks angles between  $\theta = 15^\circ$  and  $\theta = 165^\circ$ .

From Figure 5(c), the convection velocity returned by the above method for the  $\theta = 15^\circ$  case is significantly greater than the convection velocity for  $\theta = 75^\circ$ . The low-drag area observed for  $\theta = 15^\circ$  means that less of a velocity defect is expected. Indeed, the ratio of convection velocities between the two cases is approximately equal to the ratio of time-averaged drag area. The smaller total area of the plane enclosed within the contour at the  $15^\circ$  case – that is to say, the weaker vortices present – is also indicative of the drag area difference. The question then is how to select a global estimate of convection velocity.

For a downstream station at  $z = 0.6$  m, an average of the velocity plotted in Figure 5 is taken up to  $z = 0.6$  m for the six crank angle cases plotted, and then the mean of those averages is calculated. The resulting estimated convection velocity is  $u_c = 0.645$ , giving a phase lag of approximately  $\theta_l \approx 30^\circ$ . This means when comparing the flow at, for example, a crank angle of  $\theta = 15^\circ$ , the data from the dynamic model are in fact taken with the crank angle set at  $45^\circ$ . This reflects that the structures observed in the time-averaged transient simulations are beginning on the surface of the rider. If the vorticity pattern generated on the static model is to be observed in the dynamic case, a correction for the convection velocity should be calculated over the entire distance to the downstream station. The correction for this phase lag is included throughout the following results and figures.

Giving an indication of the sensitivity of the calculation to the vortex-edge definition, Figure 6 plots the variation of convection velocity with the vortex boundary identification criterion, which is an absolute value of streamwise vorticity, for the  $15^\circ$  and  $75^\circ$  crank angle cases.

The plot gives an indication of the sensitivity of the calculated convection velocity to where the vortex edge criterion is set. It indicates that the criterion used for the vortex edge,  $|\bar{\omega}_z| = 33 \text{ s}^{-1}$ , is near the middle of the range of convection velocity estimates. The process is partly subjective, with the criterion depending on a qualitative assessment of the vorticity topology. Nonetheless, the estimation of the convection velocity can be tested by observing downstream vorticity planes and comparing them between the different methodologies.

### Vorticity planes

Figure 7 presents the vorticity fields downstream of the cyclist from the dynamic simulation across the crank angle cycle. Due to the computational expense of the simulation, only approximately seven cycle periods are available, resulting in six or seven samples to each average, as indicated on the figure (where  $T$  is the period of the cycle). The first row of images represents one half

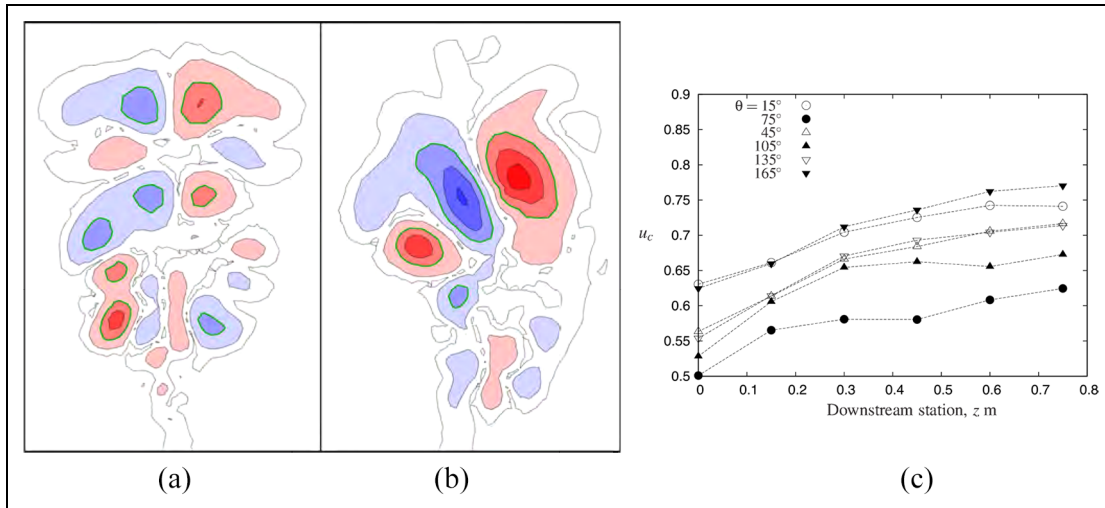


**Figure 5.** From transient simulations of flows past static cyclist models, plots of time-averaged streamwise vorticity, for (a)  $\theta = 15^\circ$  and (b)  $\theta = 75^\circ$ . On each, a green line indicates the contour at which the edge of the vortex is assumed. (c) Plots the average of the streamwise velocity in the regions contained within the contour level corresponding to a time-averaged streamwise vorticity  $|\bar{\omega}_z| = 33 \text{ s}^{-1}$ , for six crank angle cases over a half cycle, across a range of downstream stations.

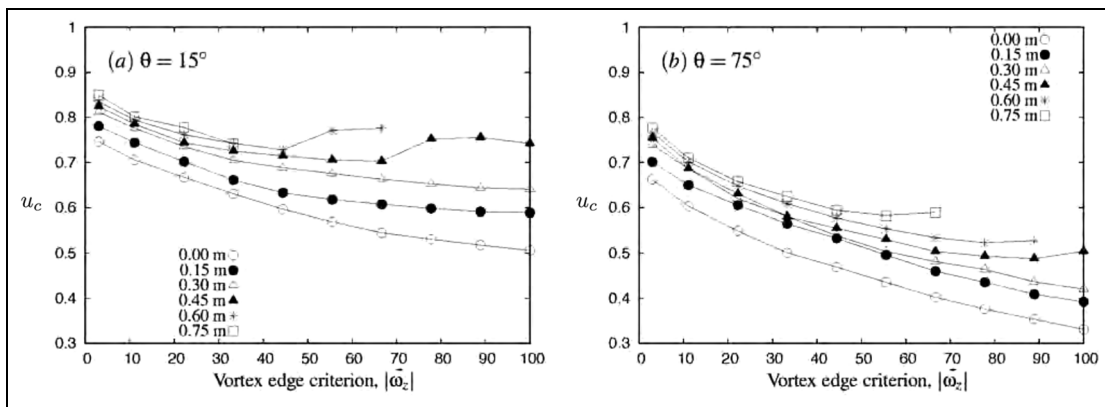


**Figure 6.** Variation of estimated convection velocity with downstream location and vortex definition criterion, for both the static model  $15^\circ$  and  $75^\circ$  cases.

of the cycle, while the second row represents the other half. The third row represents the same half of the cycle as the first row, but includes mirror images from the other half of the cycle, providing more sample points for the average. What the fields show is a switching of the wake from one half of the rider to the other as expected from previous studies.<sup>11</sup> The symmetry of the solution can be qualitatively assessed by comparing flow fields  $180^\circ$  apart: these flows will ideally be mirror images of one another. In most cases, a symmetry can be observed in the orientation of the main vortex pair, such as in the  $75^\circ$ – $255^\circ$ ,  $135^\circ$ – $315^\circ$  and  $165^\circ$ – $345^\circ$  pairs. The presence of this switching indicates that the side-ways bias exhibited in flows for static models is relevant for pedalling cyclist flows.

For the  $15^\circ$ – $195^\circ$  pair, there is not a close symmetry. In this case, it is important to be aware of the limited crank angle cycles available for the phase averaging. As was observed previously<sup>12</sup> for static crank angle

simulations, these crank angles seem to produce highly variable flows that require considerable time to attain the converged average state. Furthermore, a global estimate of the convection velocity has been applied. In reality, different parts of the vorticity topology at the downstream plane have their origins at different parts of the rider surface. The main vortices begin from the torso, but smaller vortices also begin from the knees and feet, which at different times are different distances upstream from the origin at  $x = 0 \text{ m}$ , thereby having a particular phase lag associated with a longer convection distance, not reflected in the global estimate calculated from Figure 5(c).

To assess the variability in the phase averages, for the  $\theta = 15^\circ$  and  $\theta = 75^\circ$  cases, Figure 8 plots three instantaneous vorticity fields that contribute to the average fields shown in Figure 7. There is a strong variation in the instantaneous field from the phase-averaged field for the low-drag  $\theta = 15^\circ$  case.

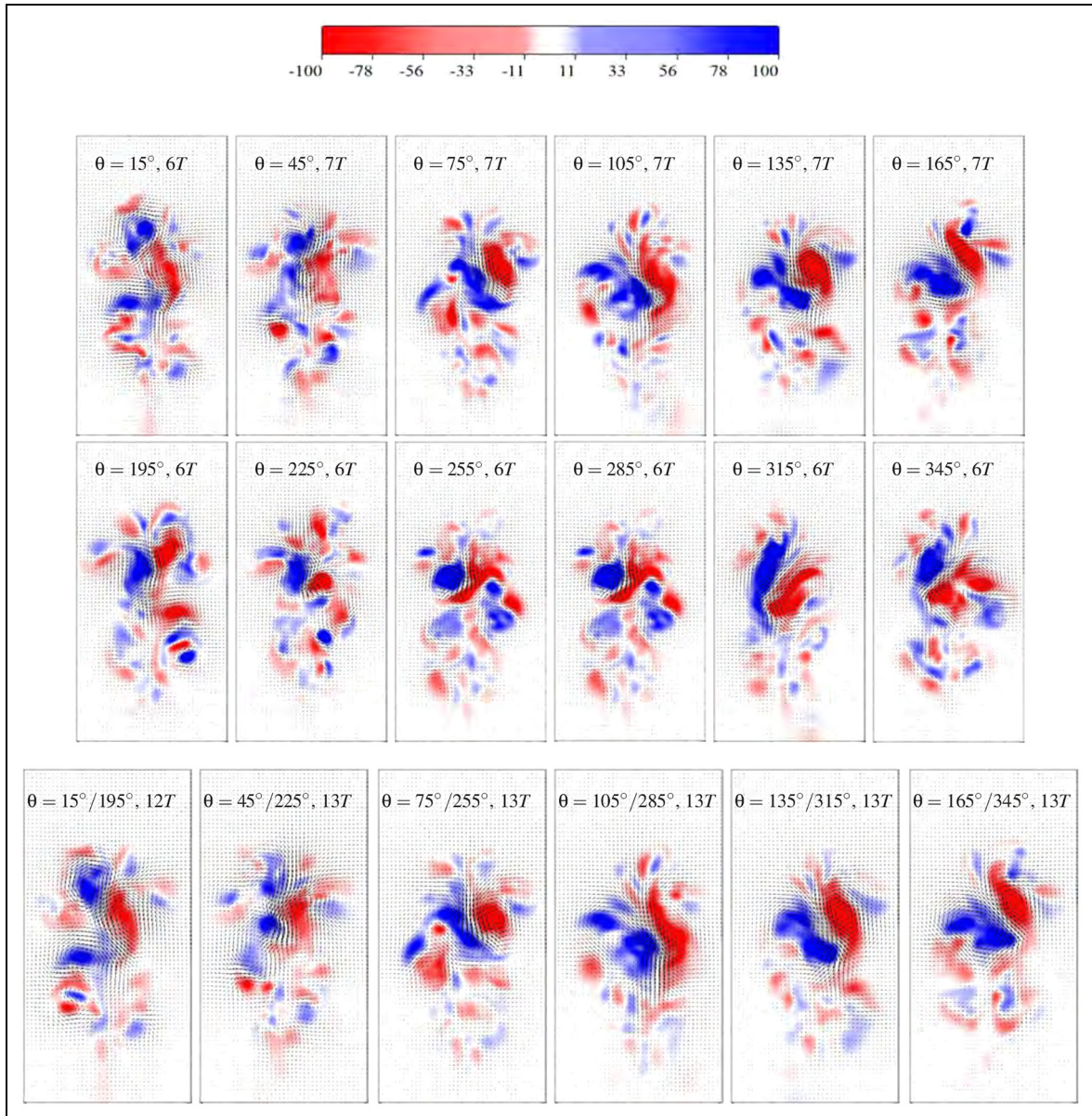


**Figure 7.** Contours of streamwise vorticity with vectors of cross-stream velocity at  $30^\circ$  increments through the crank cycle, phase-averaged from the dynamic simulation. The first and second rows show the results over the entire cycle. The number of crank angle cycles included in each phase average is indicated on each image. The third row is the average over half the cycle, including the mirror images of the second half of the cycle, resulting in a higher sample count, but relying on symmetry in the flow solution. Results are shown from the  $x = 0.60$  m (downstream of the rear of the cyclist) cross section and include correction for a phase lag of  $30^\circ$  to account for the downstream distance. Contours vary across the range  $-100 \leq \omega_x \leq 100 \text{ s}^{-1}$ , as shown by the colour bar. *Note.* The vorticity contours for the last row should be mirrored and reversed in sign for the second marked angles.

Qualitatively, there is little similarity between the three instantaneous fields. By contrast, the  $\theta = 75^\circ$  case shows a strong similarity between the average and the instantaneous field. In each image, a larger vortex pair is present, biased towards the right-hand side of the rider. This variation in similarity exists across the range of crank angle plotted in Figure 7. It is strongest in the cases where there exists a stronger vortex pair, biased to one side – for example, in the cases corresponding to crank angles between  $\theta = 75^\circ$  and  $\theta = 165^\circ$ . For other cases, such as those corresponding to crank angles  $\theta = 15^\circ$  and  $\theta = 45^\circ$ , a much higher variation is

present. Figures 7 and 8 depict a wake that is shifting from side to side as the crank angle varies. During the high-drag phases, the wake is biased to one side and relatively consistent from one cycle to the next. The transition of the wake from one side of the rider to the other is less consistent, with the transition phases of approximately  $\theta = 0^\circ$  to  $\theta = 60^\circ$  ( $\theta = 180^\circ$  to  $240^\circ$ ) varying from cycle to cycle. The snapshots plotted here are snapshots of that transition. Increasing the number of pedal cycles over which phase-averaged results are obtained has the potential to improve these results, but this is computationally expensive.

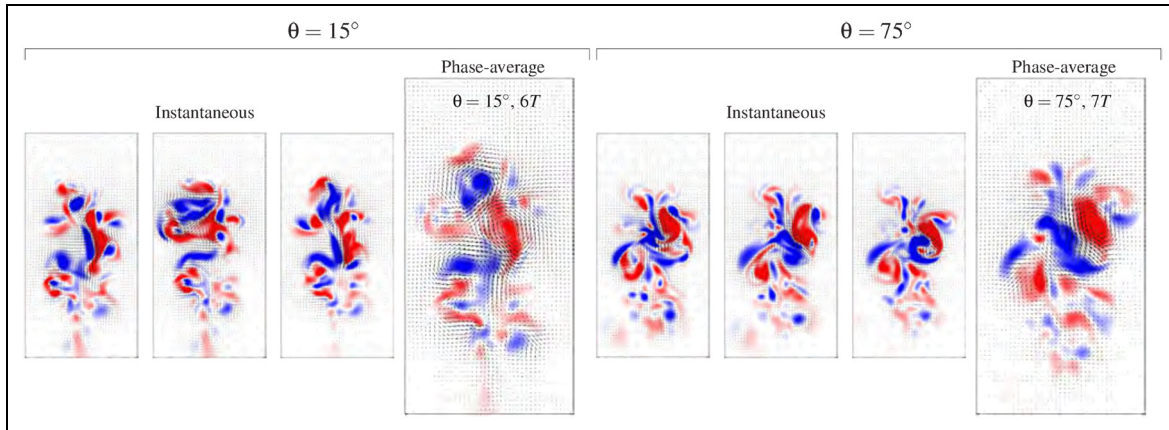


**Figure 8.** Contour plots of streamwise vorticity at downstream location  $x = 0.6$  m, for crank angles cases  $\theta = 15^\circ$  and  $\theta = 75^\circ$ . Three instantaneous fields are shown for each case, with the phase-averaged field shown to the right in each case.

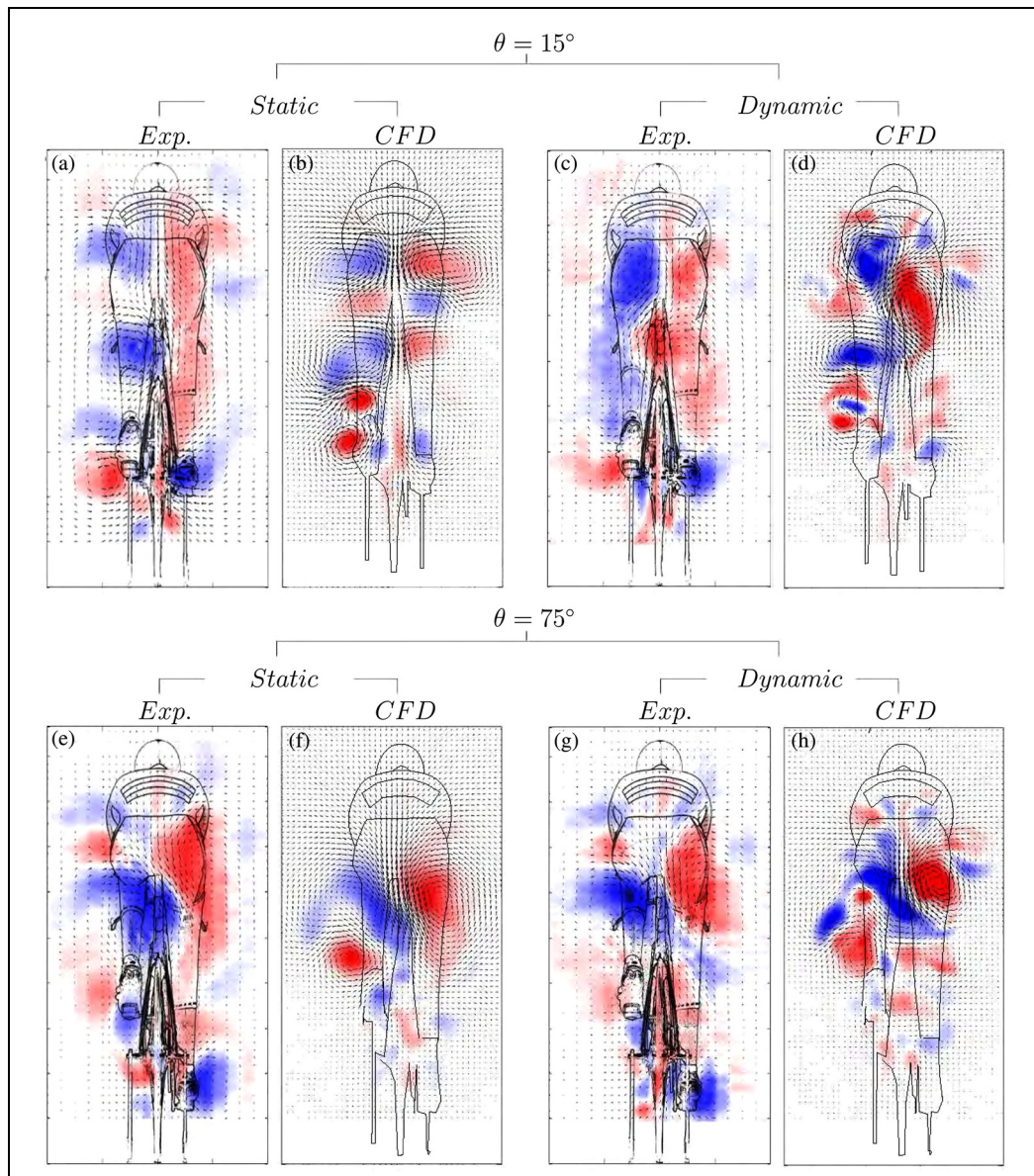
Figure 9 summarises results across the various methodologies employed, comparing the four sets of data available for the low- and high-drag cases at  $\theta = 15^\circ$  and  $\theta = 75^\circ$ , respectively, for time-averaged wind-tunnel velocity probe data for static models, time-averaged transient CFD solutions for static models and phased-averaged results for the pedalling experimental and numerical studies. For the two crank angles shown, the good comparison explored<sup>12</sup> previously between the experimental results and the time-averaged transient CFD solution can be seen in the two leftmost columns of each set, that is, between (a) and (b) for  $\theta = 15^\circ$  and between (e) and (f) for  $\theta = 75^\circ$ . The numerical results have a much higher spatial resolution than the experiments and can resolve much smaller structures. The large-scale structures are captured well in the simulations, particularly for the asymmetric  $75^\circ$  leg position.

Figure 9(d) and (h) shows results of the simulated phase-averaged vorticity fields about the low- and high-drag leg positions, which are compared with their experimental counterpart in (c) and (g), respectively. For the low-drag case of  $\theta = 15^\circ$ , the balanced vortex structure seen in the static simulations and experiments is not seen in the dynamic simulation. The asymmetry in the two primary streamwise vortices is captured in both experiment and simulation. Both data sets suggest that the flipping of the wake is shifted to later stages of the crank cycle compared to the static cases. This is a positive result given the limited number of crank cycles that phased-averaged numerical results comprises. For the high-drag  $\theta = 75^\circ$  case, the correlation between the dynamic and experimental phase-averaged flow field results is strong. Although the flow is less sharply defined than for the time averages, the dominant vortex pair is identified with the same sideways bias as observed in the experiments.

## Conclusion

Full-scale, time-mean RANS simulations of the flow past a bicycle/rider combination for different static leg

positions have been extended to the more computationally challenging dynamic pedalling case based on the unsteady SAS-SST turbulence model. The complexity of the simulation is mainly due to the large-scale, surface-intersecting model deformation, requiring regular remeshing (360 times) throughout the crank cycle. A comparison of simulations using different remeshing time increments suggests that the induced overall uncertainty in instantaneous drag is of the order of 2% due to remeshing. This should be compared to the total drag variation of  $\sim 20\%$  over the entire cycle, which takes place as the leg position moves from the low-drag state at  $15^\circ$  to the high-drag state at  $75^\circ$ . The simulation allowed the mapping of the variation of drag with crank angle. Through the cycle, the drag area returned by the dynamic simulation was 5%–10% less than the drag areas returned by the time average of transient static leg simulations. Compared with experimental findings, this variation in static and dynamic results is expected over approximately the first and third quarters of a full crank cycle. In other portions of the crank cycle, the simulated results showed similar trends between static and dynamic results, as found in experiment, but did not completely capture the ‘redistribution’ of  $C_D A$  to levels above static results. In addition to numerical errors arising from the remeshing technique and the limited number of cycles simulated, it is expected that the simplification in the geometry of the numerical model, particularly the localised areas around the hip and knee joints compared to the experimental mannequin, is the main contributor of this difference in findings. The simulations also show good qualitative similarity in the wake vorticity fields, observed at selected crank angles between time-averaged static-model simulations and phase averages from the dynamic simulation, despite the limited number of pedalling cycles (seven) simulated and used for phase averaging. The numerical methods described offer a viable option to use computational simulation to assess the aerodynamic performance of cyclist over a complete crank cycle as opposed to an isolated static



**Figure 9.** Contours of streamwise vorticity with vectors of cross-stream velocity for a cyclist at crank angle of  $15^\circ$  (a–d) and  $75^\circ$  (e–h), at cross section  $x = 0.60$  m. Streamwise vorticity fields are shown for (a) and (e) static experimental transient average, (b) and (f) static numerical transient average, (c) and (g) phase-averaged dynamic experimental results and (d) and (h) phase-averaged numerical results. The dynamic result shown here is the average over both sides of the crank cycle; therefore, included here are the mirror images of the results at  $\theta = 195^\circ$  and  $\theta = 255^\circ$ . Included in the dynamic results is the appropriate phase shift for the downstream distance. Contours vary across the range  $-100 \leq \omega_x \leq 100 \text{ s}^{-1}$ .

leg position, which is currently the norm and clearly has its limitations.

#### Declaration of conflicting interests

The author(s) declared no potential conflicts of interest with respect to the research, authorship, and/or publication of this article.

#### Funding

The author(s) disclosed receipt of the following financial support for the research, authorship, and/or publication of this article: This work was supported by the Australian Research Council, through the Linkage Project

scheme (project numbers: LP100200090, LP130100955) and through the Australian Institute of Sport. The work was also supported by awards under the Merit Allocation Scheme (project d71) on the NCI National Facility at the Australian National University.

#### ORCID iD

Timothy N Crouch  <https://orcid.org/0000-0001-8208-0101>

#### References

1. Grappe G, Candau R, Belli A, et al. Aerodynamic drag in field cycling with special reference to the Obree's position. *Ergonomics* 1997; 40: 1299–1311.

2. Kyle CR and Burke E. Improving the racing bicycle. *Mech Eng* 1984; 105(9): 34–35.
3. Defraeye T, Blocken B, Koninckx E, et al. Aerodynamic study of different cyclist positions: CFD analysis and full-scale wind-tunnel tests. *J Biomech* 2010; 43: 1262–1268.
4. Defraeye T, Blocken B, Koninckx E, et al. Computational fluid dynamics analysis of cyclist aerodynamics: performance of different turbulence-modelling and boundary-layer modelling approaches. *J Biomech* 2010; 43: 2281–2287.
5. Defraeye T, Blocken B, Koninckx E, et al. Computational fluid dynamics analysis of drag and convective heat transfer of individual body segments for different cyclist positions. *J Biomech* 2011; 44: 1695–1701.
6. Blocken B, Defraeye T, Koninckx E, et al. CFD simulations of the aerodynamic drag of two drafting cyclists. *Comput Fluids* 2013; 71: 435–445.
7. Defraeye T, Blocken B, Koninckx E, et al. Cyclist drag in team pursuit: influence of cyclist sequence, stature, and arm spacing. *J Biomed Eng* 2014; 136: 011005.
8. Blocken B and Toparlar Y. A following car influences cyclist drag: CFD simulations and wind tunnel measurements. *J Wind Eng Ind Aerod* 2015; 145: 178–186.
9. Fintelman DM, Hemida H, Sterling M, et al. CFD simulations of the flow around a cyclist subjected to crosswinds. *J Wind Eng Ind Aerod* 2015; 144: 31–41.
10. Fintelman DM, Sterling M, Hemida H, et al. The effect of crosswinds on cyclists: an experimental study. *Proced Eng* 2014; 72: 720–725.
11. Crouch T, Burton D, Brown N, et al. Flow topology in the wake of a cyclist and its effect on aerodynamic drag. *J Fluid Mech* 2014; 748: 5–35.
12. Griffith MD, Crouch T, Thompson MC, et al. Computational fluid dynamics study of the effect of leg position on cyclist aerodynamic drag. *J Fluid Eng* 2014; 136(10): 101105.
13. Crouch TN, Burton D, Thompson MC, et al. Dynamic leg-motion and its effect on the aerodynamic performance of cyclists. *J Fluids Struct* 2016; 65: 121–137.
14. Von Loebbecke A, Mittal R, Mark R, et al. A computational method for analysis of underwater dolphin kick hydrodynamics in human swimming. *Sports Biomech* 2009; 8(1): 60–77.
15. Menter FR and Egorov Y. The scale-adaptive simulation method for unsteady turbulent flow predictions. Part 1: theory and model description. *Flow Turb Combust* 2010; 85: 113–138.
16. Egorov Y, Menter FR and Cokljat D. The scale-adaptive simulation method for unsteady turbulent flow predictions. Part 2: application to aerodynamic flows. *Flow Turb Combust* 2009; 85: 139–165.
17. Duda B, Menter F, Deck S, et al. Application of the scale-adaptive simulation to a hot jet in cross flow. *AIAA J* 2013; 51(3): 052021.